Research Article Vol. 13, No. 6 / June 2026 / Optica 1035

Chip-based 16 GBaud continuous-variable quantum key distribution

Adnan A. E. Hajomer,[1,†,*] Axl Bomhals,[2,†] Cédric Bruynsteen,[2] Aboobackkar Sidhique,[2] Olena Kovalenko,[3] Ivan Derkach,[3] Vladyslav C. Usenko,[3] Ulrik L. Andersen,[1] Xin Yin,[2,4] and Tobias Gehring[1,5]

[1]Center for Macroscopic Quantum States (bigQ), Department of Physics, Technical University of Denmark, 2800 Kongens, Lyngby, Denmark
[2]Ghent University-imec, IDLab, Dep. INTEC, Ghent 9052, Belgium
[3]Department of Optics, Faculty of Science, Palacky University, 17. listopadu 12, Olomouc 771 46, Czech Republic
[4]xin.yin@ugent.be
[5]tobias.gehring@fysik.dtu.dk
[†]These authors contributed equally to this work.
[*]aaeha@dtu.dk

Received 20 January 2026; revised 23 April 2026; accepted 4 May 2026; published 27 May 2026

Quantum key distribution (QKD) stands as the most successful application of quantum information science, providing information-theoretic security for key exchange. While it has evolved from proof-of-concept experiments to commercial products, widespread adoption requires chip-based integration to reduce costs, enable mass production, facilitate miniaturization, and enhance system performance. Here, we demonstrate a fully photonic-integrated continuous-variable QKD (CV-QKD) system operating at a classical telecom symbol rate of 16 GBaud. Our system integrates a silicon photonic transmitter circuit (excluding the laser source) and a 20 GHz shot-noise-limited photonic–electronic receiver, which features a phase-diverse silicon photonic integrated circuit and custom-designed GaAs pHEMT transimpedance amplifiers. Advanced digital signal processing allows our system to achieve a secure key rate for discrete-modulated coherent state CV-QKD that reaches 0.289 Gb/s and 0.246 Gb/s over a 20 km fiber link in the asymptotic regime and with finite-size parameter estimation, respectively. These results represent a critical step toward scalable, cost-effective, and mass-deployable quantum-secure communication using photonic-integrated CV-QKD systems.

https://doi.org/10.1364/OPTICA.590832

1. INTRODUCTION

Quantum key distribution (QKD), the cornerstone of quantum communication, enables the secure exchange of cryptographic keys over public channels with information-theoretic security [1,2], making it resistant to attacks from both classical and quantum computers. While QKD has transitioned from a theoretical concept to real-world implementations, including field trials and commercial products [3], its widespread adoption is still hindered by scalability, network integration challenges, and high manufacturing costs [4]. Photonic integration is a key enabler for overcoming these limitations, allowing for miniaturization, cost reduction, mass production, and enhanced system performance [5]—particularly in achieving high secure key rates necessary for modern data-intensive applications.

Among various QKD implementations, continuous-variable QKD (CV-QKD) is particularly well suited for photonic integration due to its inherent compatibility with standard telecommunications technologies [6]. In CV-QKD, information is encoded in the continuous degrees of freedom of a quantum system—such as the amplitude and phase quadratures of the electromagnetic field of light—using a quadrature modulator and decoded via coherent detection [7]. These core operations of encoding and decoding can be efficiently implemented in integrated photonic circuits fabricated using standard foundry processes. Furthermore, CV-QKD can achieve high secure key rates, approaching the Pirandola–Laurenza–Ottaviani–Banchi (PLOB) bound [8], making it well suited for high-data-rate quantum-secured communication.

However, despite its intrinsic compatibility with photonic integration, most prior efforts have focused on integrating individual system components rather than developing a fully integrated CV-QKD solution [9–13]. Although Zhang *et al*. [14] demonstrated an integrated CV-QKD system, their secure key rate was limited to 250 kbit/s due to a limited system bandwidth. Moreover, their system transmitted the local oscillator and quantum signal through the same fiber, a configuration known to be susceptible to implementation loopholes. This underscores the pressing need for high-performance, chip-based CV-QKD systems that can achieve higher secure key rates for practical deployment.

In this work, we report the fastest integrated CV-QKD system to date (excluding the laser source), operating at a symbol rate of 16 GBaud. Our photonic-integrated transmitter incorporates a

silicon photonic in-phase and quadrature (IQ) modulator with a 3 dB bandwidth of 7 GHz, enabling high-speed quantum state encoding. Meanwhile, our photonic-electronic-integrated receiver features a silicon photonic phase-diverse coherent detector, complemented by custom-designed GaAs pHEMT transimpedance amplifiers, achieving quantum noise-limited detection across a 20 GHz bandwidth. By combining these integrated subsystems with advanced digital signal processing (DSP) techniques, including pre- and post-equalization [15], we achieve record-breaking secure key rates of 0.289 Gb/s in the asymptotic regime and 0.246 Gb/s with the finite-size parameter estimation over a 20 km fiber link. These results mark a significant step forward in the development of scalable, high-speed, and cost-effective CV-QKD systems, demonstrating the transformative potential of photonic integration in enabling the mass deployment of quantum-secured communication networks.

2. INTEGRATED CV-QKD SYSTEM

Our integrated CV-QKD system comprises an integrated transmitter and receiver fabricated using imec's ISiPP50G silicon platform [16]. Figure 1(a) illustrates the photonic integrated circuit (PIC) of our transmitter, highlighting its core components: an IQ modulator for optical signal modulation, a Mach–Zehnder interferometer (MZI) designed for adjusting IQ amplitude imbalance, and a photodiode for signal monitoring.

The IQ modulator consists of two parallel Mach–Zehnder modulators (MZMs) with a voltage-length product ($V_\pi L$) of 1.7 V·cm, utilizing multi-mode interferometers (MMIs) for efficient light splitting and combining. Each MZM incorporates a depletion-mode phase shifter optimized for high-frequency operation, along with tungsten waveguide heaters for bias point control, operating together in a push-pull configuration. To achieve the required 90° phase shift between the I and Q branches, additional heaters are integrated within the IQ modulator structure. Figure 1(b) shows the S_{21} measurement of the nested MZMs and PCB transmission lines, revealing a similar frequency response and a 3 dB bandwidth of 7 GHz.

A printed circuit board, shown in Fig. 1(c), is used to make electrical connections to the PIC for RF and DC signals. These connections are wire-bonded to the PIC. The DC bias voltages for two MZM heaters and a 90 deg phase-shifting heater are connected to a DB25 connector for automatic bias control. The DC traces from the fourth heater in the MZI are connected to headers for manual tuning, along with the anode and cathode traces of the monitor photodetector. The RF inputs to the modulator are wire-bonded to match differential traces on the PCB and utilize a multicoax connector (Ardent TR40) for external connection. A polarization-maintaining fiber array with ultra-high numerical aperture fiber is employed to couple light into and out of the edge couplers of the PIC transmitter. Two additional edge couplers, connected to a known optical channel, are used to align the fiber array with the help of a six-axis stage. The fiber array was glued with a low-loss adhesive for mechanical stability. The insertion loss of the edge coupler is 8 dB, which is still quite high. With

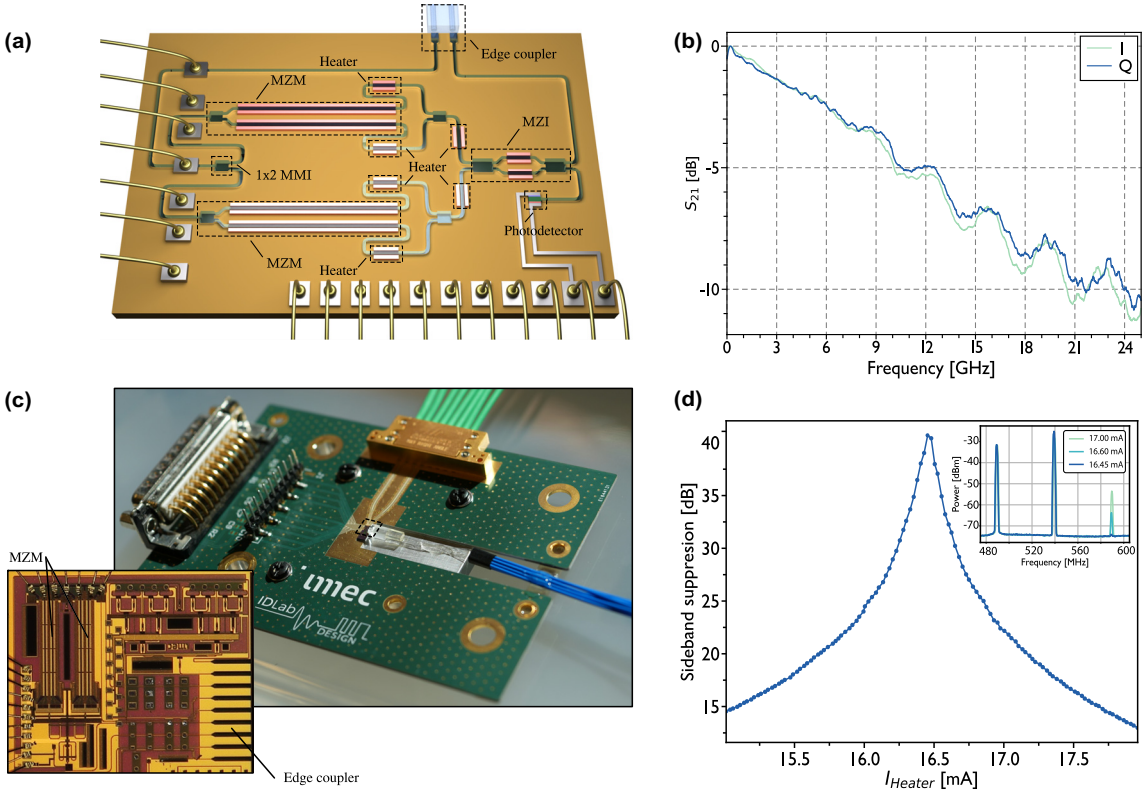

Fig. 1. Transmitter chip. (a) Functional diagram of the photonic integrated circuit IQ modulator. (b) Frequency response of the nested Mach–Zehnder modulators (MZMs) and the printed circuit board (PCB) transmission lines, as determined by the S_{21} parameter. (c) Micrograph of the IQ modulator photonic integrated circuit mounted on its PCB. (d) Sideband suppression as a function of the heater driving current in the cascaded Mach–Zehnder interferometer (MZI). The inset shows the spectra at three representative heater currents while driving the modulator with a 50 MHz signal, revealing the main sideband, beat signal, and suppressed sideband at approximately 490, 540, and 590 MHz, respectively, with corresponding suppression levels of 40, 22, and 28 dB. MMI, multimode interferometer.

improvements in the alignment process, especially during the curing of the glue, this loss could be further reduced to 3 dB, as seen before curing. However, these losses are not critical to the system, as the output of the modulator is strongly attenuated to achieve the desired modulation variance.

Our transmitter can operate in various modes depending on the driving bias voltages and RF signals. A particularly important mode for CV-QKD is the optical single-sideband suppressed-carrier mode [17,18]. Ideally, when both MZMs are biased at the minimum transmission, maintaining a 90° phase shift and equal amplitude for both I and Q quadratures, the carrier and one of the sidebands can be effectively suppressed. However, maintaining a perfect amplitude balance between the I and Q branches is challenging due to manufacturing tolerances. This imbalance can degrade sideband suppression performance, potentially resulting in a security loophole [19,20]. Additionally, it distorts the symmetry of the modulation constellation in phase space, complicating phase carrier recovery and degrading system performance [21]. To address this issue, we integrated an additional MZI with a pair of heaters specifically designed to correct amplitude imbalances between the two modulated quadratures. As shown in Fig. 1(d), by tuning these heaters, a sideband suppression of 40.7 dB was achieved. Additionally, a photodiode is included to monitor and stabilize the MZI operation.

Our phase-diverse receiver optical front-end, shown as inset (b) in Fig. 2, is also fabricated using imec's iSiPP50G silicon photonics platform. It couples light into the chip via two grating couplers and uses a 1 × 2 MMI to split the quantum signal and local oscillator (LO) into two arms, enabling the measurement of conjugate quadratures. Two waveguide heaters ensure a 90° phase shift between arms, followed by balanced homodyne detectors composed of a MZI and high-responsivity photodetectors. Each pair of balanced photodetectors was connected to a separate TIA, custom-designed in a 100 nm GaAs pHEMT process. The integrated photonic and electronic receiver provides a shot-noise-limited bandwidth of 20 GHz and achieves an efficiency of 44%. For further details on the optical front-end design and the integrated transimpedance amplifier of our receiver, we refer the reader to Refs. [15,22] and to the Supplement 1 of Ref. [15] for receiver characterization.

3. HIGH-RATE CV-QKD SYSTEM

Figure 2 shows our high-speed, chip-based CV-QKD system, which implements a discrete-modulated (DM) CV-QKD protocol [23]. The system consists of a transmitter (Alice) and a receiver (Bob), connected through a quantum channel composed of standard single-mode fiber (SSMF). The following sections provide a detailed description of the system components.

A. Transmitter (Alice)

At Alice's station, a 1550 nm continuous-wave (CW) laser with a narrow linewidth of 100 Hz served as the optical source. The coherent states were generated using our integrated IQ modulator, which was driven by an 8-bit arbitrary waveform generator (AWG,

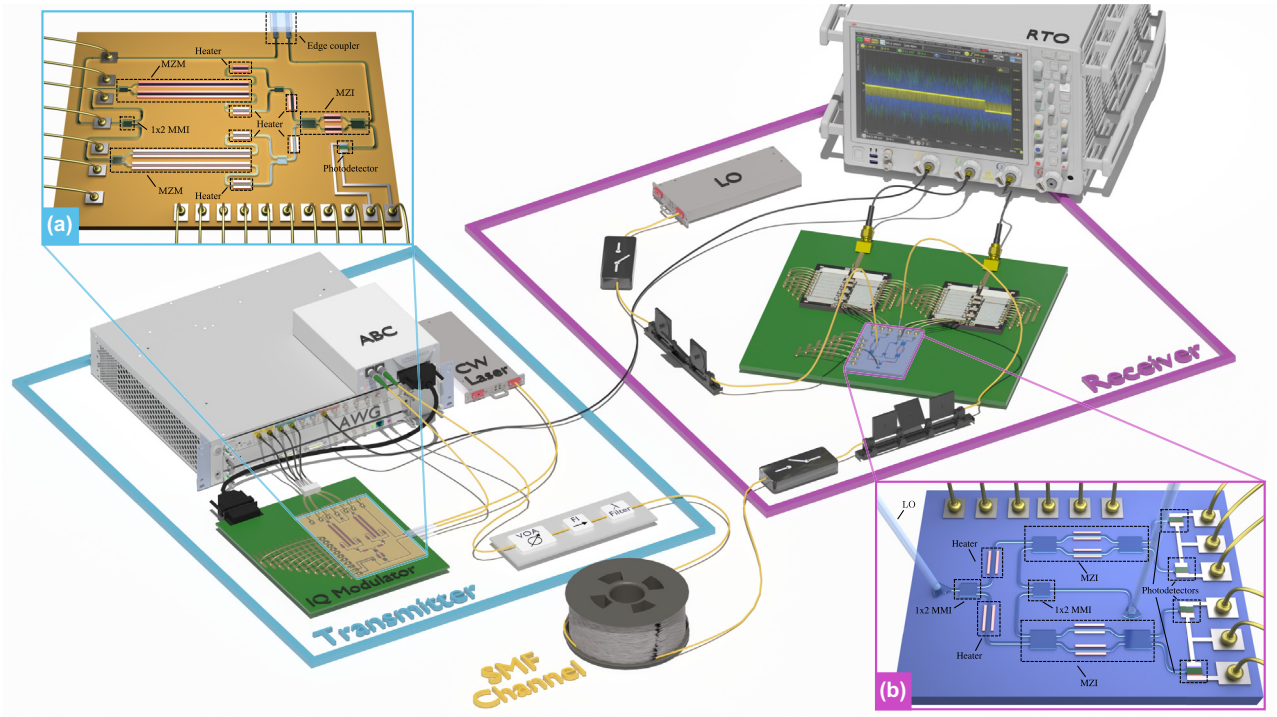

Fig. 2. Experimental setup of the high-speed CV-QKD system. The transmitter prepares coherent states using a continuous-wave (CW) laser at a telecom wavelength of 1550 nm, which is modulated by our integrated IQ modulator [inset (a)] driven by a high-speed arbitrary waveform generator (AWG). An automatic bias controller (ABC) stabilizes the IQ-modulator bias voltages, while a variable optical attenuator (VOA) sets the modulation variance. To mitigate Trojan-horse attacks, a Faraday isolator (FI) and a wavelength-selective filter are placed at the transmitter output. On the receiver side, a CW laser serves as the local oscillator (LO) for coherent detection. The setup includes optical switches for calibration, manual polarization controllers to optimize coupling into the chip, and our integrated photonic–electronic phase-diverse receiver mounted on a similar dark-green interposer PCB. Inset Fig. 2(b) shows the optical front-end of the receiver. Finally, the signal is digitized using a real-time oscilloscope (RTO). MZI, Mach–Zehnder interferometer; MMI, multimode interferometer; and SMF, single-mode fiber.

Keysight M8195A) operating at a sampling rate of 32 GSa/s. The bias voltages of the modulator were controlled by a commercial automatic bias controller combined with a customized buffer circuit consisting of common-emitter followers to stably drive the heaters. The modulation variance of the transmitted quantum states was adjusted using a variable optical attenuator (VOA) and by tuning the AWG driving voltage. To prevent back-reflections and mitigate potential Trojan-horse attacks, a Faraday isolator and optical filter were placed at the transmitter's output.

The complex amplitude of each coherent state, $|\alpha\rangle = |x + jp\rangle$, was randomly selected at a rate of 16 GBaud from a probabilistically shaped discrete constellation with a predefined modulation order (M) and a Gaussian-like probability distribution. The quantum symbols were upsampled to match the AWG sampling rate and pulse-shaped using a root-raised cosine (RRC) filter with a roll-off factor of 0.2. To support the high symbol rates, a pre-emphasis filter was applied to compensate for the high-frequency roll-off of the transmitter, with coefficients derived from the inverse transfer function of the transmitter [15]. Additionally, a 15 GHz pilot tone was frequency-multiplexed with the quantum signal to establish a phase reference between the transmitter and receiver.

B. Receiver (Bob)

At the receiver, the coherent states were measured using an intradyne detection scheme [15,24]. This scheme employed our integrated phase-diverse receiver along with a free-running CW laser serving as the local oscillator (LO), which operated independently of Alice's laser. To avoid degradation from the vacuum mode in the image sideband, the frequency offset between the two lasers was maintained below half the quantum signal bandwidth. Two polarization controllers (PCs) were used to align the LO and the quantum signal for optimal coupling into the receiver chip. Additionally, two optical switches, each with a switching time of approximately 5 ms, were incorporated in the LO and signal paths to enable vacuum noise and electronic noise calibration. The resulting system stability was verified to exceed 1 min by computing the Allan deviation of consecutive vacuum measurements. Following the detection, the signal was digitized using an 8-bit real-time oscilloscope (RTO, Keysight DSA Z634A) operating at 80 GSa/s, synchronized with the AWG via a 100 MHz reference clock. However, digital clock recovery can also enable asynchronous operation [25]. The digitized signals were subsequently processed offline.

To recover the quantum symbols, an initial frequency-domain equalizer (whitening filter) was applied to compensate for the high-frequency roll-off of the receiver. The filter coefficients were determined from the inverse frequency response obtained via vacuum noise measurements. The frequency offset between Alice's and Bob's lasers was estimated using the Hilbert transform of the pilot tone, followed by a linear phase fit of the extracted phase profile. The relative phase was then determined by shifting the pilot tone to baseband using the estimated frequency offset. The quantum signal was then transformed to baseband and corrected for phase. Operating at 16 Gbaud results in fewer samples per symbol, which makes accurate time synchronization challenging. To address this, we added a new DSP module that digitally oversamples the signal. We then perform cross-correlation between the transmitted and received reference sequences to compensate for propagation delays introduced by the fiber link and electronic components. Finally, after matched filtering and downsampling, the quantum symbols were reconstructed for further processing.

4. RESULTS

The security of CV-QKD is evaluated using the Devetak–Winter bound, quantifying the information advantage that trusted parties (Alice and Bob) have over an eavesdropper (Eve) controlling the quantum channel. The bound is defined as $R = \beta I(A:B) - \chi(E:B)$, where $I(A:B)$ is the mutual information between Alice and Bob, calculated directly from their encoded and measured data, and closely related to the signal-to-noise ratio (SNR). The mutual information is limited by the efficiency of information reconciliation $\beta \in [0, 1]$. The secure key R is commonly scaled down by the frame error rate $(1 - \mathrm{FER})$; however, here we presume it to be absent $\mathrm{FER} = 0$. The second term, $\chi(E:B)$, is the Holevo bound, representing the maximum information Eve can obtain considering collective attacks [6]. Under the assumption of a Gaussian quantum channel, $\chi(E:B)$ can be evaluated from two experimentally estimated parameters: the channel transmittance η and the excess noise ε. Alleviating the Gaussian channel assumption requires analyzing first and second moments of transmitted and received letters of the encoding alphabet individually. The analysis results in correlation coefficients c_1, c_2 which, along with the second moments of the received state n_B [23], allow to lower-bound the correlations between Alice and Bob in the entanglement-based representation of the protocol, and consequently to upper bound the information of Eve.

A key system parameter controlled by the sender is the modulation variance V_M, defining both the alphabet size and the resulting SNR. Optimizing V_M is crucial for achieving a positive key rate R under practical reconciliation efficiency $\beta < 1$ [17]. However, increasing V_M also amplifies residual phase noise [17,26], limiting the modulation variance. Conversely, a low V_M reduces the phase noise and, crucially, allows the protocol to closely approximate the performance of Gaussian-modulated CV-QKD using a finite number of discrete states displaced according to a continuous, zero-mean Gaussian distribution [23].

In this work, we operate our system in the low modulation variance regime, i.e., $V_M \lesssim 1$ shot-noise unit (SNU), using discrete, probabilistically shaped constellations of 16 and 64 states. These constellations are, respectively, optimized for modulation variances around $V_M \approx 1$ SNU. Security is first evaluated in the asymptotic regime, using an analytical bound for arbitrary modulations under the Gaussian channel assumption [23].

We conduct 36 measurements over a 10 km fiber link using constellations of $M = 16$ and $M = 64$, with dispersions $v_{16} = 0.215$ and $v_{64} = 0.129$, respectively. These measurements span a range of modulation variances, allowing us to examine their effect on the resulting excess noise ε and overall security of the protocol, assuming a reconciliation efficiency of $\beta = 95\%$.

Figures 3(a) and 3(b) show the secret key rate (SKR) and excess noise as a function of modulation variance for the 16-state constellation. Each data point represents an average over multiple measurements. We compare the performance of the discrete modulation protocol, in terms of the average rate $\overline{\mathrm{SKR}}$, with that of the CV Gaussian no-switching protocol [27], whose corresponding SKR is indicated by arrows in the plot. The average excess noise $\bar{\varepsilon}$ observed at the channel output is also reported, along with finite-size Gaussian bounds for parameter estimation with a misestimation probability $\varepsilon_{\mathrm{PE}} = 10^{-10}$ [28].

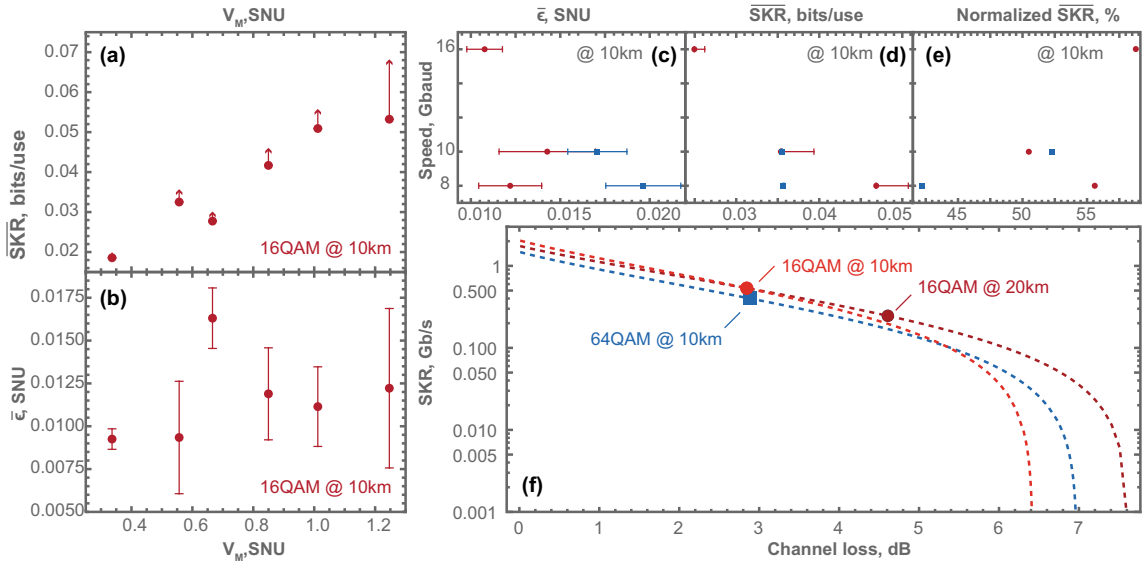

Fig. 3. Security analysis results. Red circles show constellation of size $M = 16$ and $v_{16} = 0.215$, (blue) squares $M = 64$ and $v_{64} = 0.129$. Reconciliation efficiency $\beta = 95\%$. (a)–(e) Averaged (over respective parameter) experimental results for 36 measurements over a 10 km fiber channel. (a) Asymptotic secure key rate (for $M = 16$ over 10 km fiber) in bits per channel use (arrows indicate maximal theoretical performance achieved with continuous Gaussian CV QKD protocol) dependency on the modulation variance V_M, and (b) respective averaged excess noise ε. Error bar size corresponds to the number of symbols averaged over, with the highest number of measurements taken at the lowest modulation variance. (c)–(e) Influence of operation speed (over 10 km fiber) on (c) average excess noise ε and average secure key rate with finite-size parameter estimation in (d) bits per channel use, and (e) average key rate at given speed normalized to the highest achieved key generation speed, which shows the relative performance variations across different speeds and constellations. (f) Three measurement results over 10 and 20 km fibers, with lines indicating theoretical projected performance with the same excess noise at the channel input. Parameters of the measurement are shown in Table 1: light red circle—the first row; blue square—second row; dark red circle—last row.

Limiting the modulation variance V_M to approximately 1 SNU or below ensures an acceptably low level of excess noise, as the effect of phase noise is minimal in this regime [17]. Notably, the performance gap between the 16-state discrete protocol and the continuous Gaussian modulation diminishes as V_M is reduced to sub-SNU levels. At such low variances, using a 64-state constellation allows the DM protocol to nearly match the performance of the continuous Gaussian protocol—see square markers in Fig. 3(d). The SKR difference between the latter two in this regime is less than 2×10^{-4} bits/use, corresponding to under 1% of relative key rate.

Figures 3(c)–3(e) illustrate the interplay between system symbol rate, excess noise, and SKR for constellations with $M = 16$ (circles) and $M = 64$ (squares). As shown in Fig. 3(c), lower-order constellations consistently result in reduced excess noise, irrespective of the operating symbol rate. This trend is likely attributed to limitations in the DAC bits resolution, which more strongly affects higher-order modulations. The effect could also be explained by a lower statistical sample per constellation point compared to 16QAM, leading to a greater uncertainty in point-wise noise estimation and thus a higher overall excess noise under a conservative parameter estimation. Notably, operating at a low modulation variance maintains a relatively constant excess noise across different symbol rates, as evidenced by the overlapping error bars.

In terms of average SKR in bits per channel use [Fig. 3(d)], the 64-state constellation, on average, yields similar or higher key rates compared to the 16-state constellation, despite generally higher excess noise. However, when considering key throughput in bits per second [Fig. 3(e)], the 16-state constellation operated at 16 GBaud demonstrates a significant advantage—achieving up to 60% higher SKR thanks to lower excess noise. Here, SKRs are normalized to the highest-performing configuration reported (see Table 1).

Table 1 further underscores the practical impact of operating speed: even if higher-order modulations offer an SKR advantage in bits per channel use, system throughput is ultimately determined by symbol rate and implementation simplicity.

Accordingly, operating in the very low modulation variance regime presents a compelling trade-off: low-order constellations such as $M = 16$ deliver comparable performance with the added benefits of robustness to implementation imperfections and high-speed operation. This highlights the practical value of discrete, low-order modulation formats for efficient and secure quantum key distribution under realistic system constraints.

Following this analysis, we focus on a 16-state constellation for measurements over a 20 km fiber link. We successfully extract a positive secure key rate, based on finite-size parameter estimation of the channel excess noise ε and transmittance η [28]. A summary of the key parameters is provided in Table 1, and the theoretical loss limit for secure operation is plotted in Fig. 3(f), alongside results from the 10 km measurements for comparison. While reconciliation efficiency is presumed to be $\beta = 95\%$, a positive key can still be extracted at $\beta \geq 65\%$. Lower efficiency can also translate into lower frame error rate [29], thus indicating that our system can operate under realistic error correction.

Additionally, we validate the assumption that the channel can be considered Gaussian, and compare the asymptotic SKR obtained with (based on estimated excess noise ε and transmittance η) and without (based on correlation coefficients c_1, c_2 and n_B [23] obtained directly from the measured data) the assumption of channel Gaussianity. For smaller constellation $M = 16$ both

Table 1. Experimental Parameters and Results[a]

Cardinality M (a.u.)	Symbol Rate (Gbaud)	Link Length (km)	Channel Loss η (a.u.)	V_M (SNU)	$V_{el.}$ (SNU)	ε (mSNU)	Number of Symbols	Asymptotic SKR (bits/use)	Finite-Size SKR (Gb/s)
16	16	10	0.519	0.667	0.150	7.3	2×10^6	0.0425	0.534
64	10	10	0.514	0.703	0.112	8.0	2×10^6	0.0486	0.400
16	8	10	0.512	1.01	0.081	3.7	2×10^6	0.0669	0.438
16	16	20	0.346	0.513	0.151	5.7	2×10^7	0.0181	0.246

[a] V_M, modulation variance; $V_{el.}$, electronic noise; and ε, excess noise; $\beta = 95\%$.

approaches yield similar results, with a 4% relative key rate difference on average. Such a key rate difference is smaller than the one obtained with the finite-size worst-case confidence intervals of the estimated Gaussian channel parameters, thus verifying that under low modulation variance in asymptotic regime, the channel can indeed be considered Gaussian. Note that larger constellations should be designed with finite data size in mind, as reliable estimation of parameters of low-probability edge points requires adjusting the distribution's probability shape rather than merely increasing the block size.

5. DISCUSSION

The large-scale deployment of secure quantum communication critically depends on the realization of chip-based QKD implementations as they offer substantial advantages in cost reduction, miniaturization, and enhanced performance. DM-CV-QKD stands out as a promising candidate for integrated photonic and electronic implementations, capable of achieving ultra-high symbol rates due to its compatibility with standard telecommunications technologies [15]. In this work, we have demonstrated the fastest integrated silicon photonic DM-CV-QKD system, to date, operating at a symbol rate of 16 GBaud. This milestone was made possible through the integration of a broadband silicon photonic transmitter circuit coupled with integrated silicon photonic and electronic receiver circuits and advanced DSP.

Table 2 summarizes previous efforts toward integrating CV-QKD systems. Most demonstrations have focused on integrating individual components or subsystems, and to date only one fully integrated silicon-based transmitter–receiver system has been reported. However, that implementation was limited by a bandwidth of just 10 MHz, restricting the secure key rate to 250 kbit/s and relying on an unsecured transmitted-LO scheme. Although [13] demonstrated an integrated transmitter—including an IQ modulator on an InP platform—the receiver still employed a low-bandwidth bulk detector, limiting the system bandwidth to 500 MHz. In contrast, our integrated architecture incorporates both photonic and electronic components and substantially outperforms prior demonstrations in terms of bandwidth and overall system performance. While our present implementation does not include an integrated VOA, the modulation variance can be effectively controlled via the DAC driving voltage, providing a practical alternative within the current system design.

Compared to our previous DM-CV-QKD speed record [15], the present system introduces several key advances. First, we integrate a broadband transmitter, enabling operation at substantially higher symbol rates. Second, the transmission distance is doubled through improvements in the DSP receiver, including an oversampling module that ensures accurate time synchronization at high baud rates. Finally, we extend the analysis to the non-Gaussian channel regime, providing a more comprehensive characterization of system performance under realistic conditions.

Although recent work [30] reports a higher key rate of 1.2 Gbit/s, this result is achieved over a shorter distance (10 km) and using a dual-polarization system. In Ref. [31], a higher key rate is also reported using bulk components; however, this system relies on Gaussian-modulated coherent states, which are more challenging to implement accurately in practical systems.

Furthermore, our system operates at room temperature, in contrast to high-speed discrete-variable QKD systems [32,33]. Despite these advancements, several opportunities remain for further improvements. On the photonic integration front, integrating a laser source remains a key next step. Promising approaches for laser integration on silicon platforms, such as transfer printing technology [34], could greatly enhance system compactness and functionality. To further advance compatibility with CMOS fabrication processes, future receiver designs will transition from GaAs pHEMT to Si bipolar or CMOS technology.

In terms of security analysis, two critical aspects warrant further exploration: extending the finite-size analysis to non-Gaussian channels, accounting for the failure probability of privacy amplification and the speed of convergence of the min-entropy [35]; and extending existing analytical security proofs to achieve composable

Table 2. List of Integrated CV-QKD Systems

Ref.	Integrated Parts	Modulation	Platform	Symbol Rate, GB
[9]	Component (laser)	Gaussian	III-V/Si_3N_4	0.25
[11]	Component (VOA)	Gaussian	Si	0.005
[13]	Subsystem (Tx without laser)	Gaussian	InP	0.016
[12]	Subsystem (balanced detector)	Gaussian	Si	0.1
[10]	Subsystem (balanced detector)	Gaussian	Si	1
[15]	Subsystem (phase-diverse receiver)	Discrete	Si/GaAs	10
[14]	Full system without laser	Gaussian	Si	0.001
Current work	Full system without laser	Discrete	Si	16

security. Additionally, achieving real-time operation is essential for practical deployment. A primary bottleneck currently lies in high-speed, high-efficiency information reconciliation, which could be addressed using rate-adaptive techniques and GPU-based implementations. Further scaling of the symbol rate is possible by better utilizing the receiver bandwidth. The main limitation stems from interleaving spurs in the ADC, which can be alleviated through improved sub-ADC calibration or analog equalization. For example, a continuous-time linear equalizer (CTLE) can enhance high-frequency components before digitization, thereby mitigating spur-induced distortions.

To this end, our work represents a significant advancement toward the practical realization of low-cost, ultra-high-rate QKD systems, paving the way for the widespread deployment of secure quantum communications.

Funding. Danish National Research Foundation (DNRF142); European Union's Horizon 2020 research and innovation programme (101017733); Czech Science Foundation (22-28254O, 21-44815L); Ministry of Education Youth and Sports (8C22002); European Union's Digital Europe programme (101091659, 101091625); European Union's Horizon Europe research and innovation programme (101114043); Innovation Fund Denmark (3200-00035B).

Acknowledgment. AAEH, ULA, and TG acknowledge support from the Danish National Research Foundation, Center for Macroscopic Quantum States (bigQ, DNRF142). This project was funded within the QuantERA II Programme (project CVSTAR) that has received funding from the European Union's Horizon 2020 research and innovation program under Grant Agreement No 101017733. ID acknowledges support from the project 22-28254O of the Czech Science Foundation. OK and VCU acknowledge support from the projects 21-44815L of the Czech Science Foundation and 8C22002 of the Czech Ministry of Education, Youth and Sports (MEYS), VCU acknowledges the project CZ.02.01.01/00/22_008/0004649 (QUEENTEC) of MEYS. We acknowledge support from the European Union's Horizon Europe research and innovation program under the project "Quantum Security Networks Partnership" (QSNP, grant agreement no. 101114043), from the European Union's Digital Europe programme (QCI.DK, grant agreement no. 101091659 and BeQCI, grant agreement no. 101091625), and from Innovation Fund Denmark (CyberQ, grant agreement no. 3200-00035B). We thank Bruno Govearts for his help with the fabrication of the assemblies used.

Disclosures. The authors declare no conflicts of interest.

Data availability. A summary of all estimated parameters and the security analysis is archived in an open-access repository and can be accessed at [36], in accordance with FAIR data principles.

REFERENCES

1. C. H. Bennett and G. Brassard, "Quantum cryptography: public key distribution and coin tossing," in *Proceedings of IEEE International Conference on Computers, Systems, and Signal Processing* (India, 1984), p. 175.
2. A. K. Ekert, "Quantum cryptography based on Bell's theorem," Phys. Rev. Lett. **67**, 661 (1991).
3. S. Pirandola, U. L. Andersen, L. Banchi, *et al.*, "Advances in quantum cryptography," Adv. Opt. Photonics **12**, 1012–1236 (2020).
4. E. Diamanti, H.-K. Lo, B. Qi, *et al.*, "Practical challenges in quantum key distribution," npj Quantum Inf. **2**, 1–12 (2016).
5. W. Luo, L. Cao, Y. Shi, *et al.*, "Recent progress in quantum photonic chips for quantum communication and internet," Light. Sci. Appl. **12**, 175 (2023).
6. V. C. Usenko, A. Acín, R. Alléaume, *et al.*, "Continuous-variable quantum communication," arXiv (2025).
7. F. Grosshans and P. Grangier, "Continuous variable quantum cryptography using coherent states," Phys. Rev. Lett. **88**, 057902 (2002).
8. S. Pirandola, R. Laurenza, C. Ottaviani, *et al.*, "Fundamental limits of repeaterless quantum communications," Nat. Commun. **8**, 15043 (2017).
9. L. Li, T. Wang, X. Li, *et al.*, "Continuous-variable quantum key distribution with on-chip light sources," Photonics Res. **11**, 504–516 (2023).
10. Y. Bian, Y. Pan, X. Xu, *et al.*, "Continuous-variable quantum key distribution over 28.6 km fiber with an integrated silicon photonic receiver chip," Appl. Phys. Lett. **124**, 174001 (2024).
11. Y. Bian, Y. Li, X. Xu, *et al.*, "Highly stable power control for chip-based continuous-variable quantum key distribution system," Opt. Lett. **49**, 2521–2524 (2024).
12. Y. Piétri, L. T. Vidarte, M. Schiavon, *et al.*, "Experimental demonstration of continuous-variable quantum key distribution with a silicon photonics integrated receiver," Opt. Quantum **2**, 428–437 (2024).
13. J. Aldama, S. Sarmiento, L. T. Vidarte, *et al.*, "Integrated InP-based transmitter for continuous-variable quantum key distribution," Opt. Express **33**, 8139–8149 (2025).
14. G. Zhang, J. Y. Haw, H. Cai, *et al.*, "An integrated silicon photonic chip platform for continuous-variable quantum key distribution," Nat. Photonics **13**, 839–842 (2019).
15. A. A. Hajomer, C. Bruynsteen, I. Derkach, *et al.*, "Continuous-variable quantum key distribution at 10 GBaud using an integrated photonic-electronic receiver," Optica **11**, 1197–1204 (2024).
16. P. Absil, K. Croes, A. Lesniewska, *et al.*, "Reliable 50 gb/s silicon photonics platform for next-generation data center optical interconnects," in *IEEE International Electron Devices Meeting (IEDM)* (2017), pp. 34.2.1–34.2.4.
17. A. A. Hajomer, I. Derkach, N. Jain, *et al.*, "Long-distance continuous-variable quantum key distribution over 100-km fiber with local local oscillator," Sci. Adv. **10**, eadi9474 (2024).
18. N. Jain, H.-M. Chin, H. Mani, *et al.*, "Practical continuous-variable quantum key distribution with composable security," Nat. Commun. **13**, 4740 (2022).
19. N. Jain, I. Derkach, H.-M. Chin, *et al.*, "Modulation leakage vulnerability in continuous-variable quantum key distribution," Quantum Sci. Technol. **6**, 045001 (2021).
20. A. A. Hajomer, N. Jain, H. Mani, *et al.*, "Modulation leakage-free continuous-variable quantum key distribution," npj Quantum Inf. **8**, 136 (2022).
21. A. A. Hajomer, A. N. Oruganti, I. Derkach, *et al.*, "Finite-size security of continuous-variable quantum key distribution with imperfect heterodyne measurement," arXiv (2025).
22. C. Bruynsteen, M. Vanhoecke, J. Bauwelinck, *et al.*, "Integrated balanced homodyne photonic–electronic detector for beyond 20 GHz shot-noise-limited measurements," Optica **8**, 1146–1152 (2021).
23. A. Denys, P. Brown, and A. Leverrier, "Explicit asymptotic secret key rate of continuous-variable quantum key distribution with an arbitrary modulation," Quantum **5**, 540 (2021).
24. K. Kikuchi, "Fundamentals of coherent optical fiber communications," J. Light. Technol. **34**, 157–179 (2015).
25. H.-M. Chin, N. Jain, U. L. Andersen, *et al.*, "Digital synchronization for continuous-variable quantum key distribution," Quantum Sci. Technol. **7**, 045006 (2022).
26. A. A. Hajomer, I. Derkach, R. Filip, *et al.*, "Continuous-variable quantum passive optical network," Light. Sci. Appl. **13**, 291 (2024).
27. C. Weedbrook, A. M. Lance, W. P. Bowen, *et al.*, "Quantum cryptography without switching," Phys. Rev. Lett. **93**, 170504 (2004).
28. L. Ruppert, V. C. Usenko, and R. Filip, "Long-distance continuous-variable quantum key distribution with efficient channel estimation," Phys. Rev. A **90**, 062310 (2014).
29. H. Mani, T. Gehring, P. Grabenweger, *et al.*, "Multiedge-type low-density parity-check codes for continuous-variable quantum key distribution," Phys. Rev. A **103**, 062419 (2021).
30. S. Q. Ng, F. Kanitschar, G. Zhang, *et al.*, "Gigabit-rate quantum key distribution on integrated photonic chips," arXiv (2025).
31. H. Wang, Y. Li, T. Ye, *et al.*, "High-rate continuous-variable quantum key distribution over 100 km fiber with composable security," Optica **12**, 1657–1667 (2025).
32. W. Li, L. Zhang, H. Tan, *et al.*, "High-rate quantum key distribution exceeding 110 Mb s–1," Nat. Photonics **17**, 416–421 (2023).
33. F. Grünenfelder, A. Boaron, G. V. Resta, *et al.*, "Fast single-photon detectors and real-time key distillation enable high secret-key-rate quantum key distribution systems," Nat. Photonics **17**, 422–426 (2023).
34. J. Justice, C. Bower, M. Meitl, *et al.*, "Wafer-scale integration of group III–V lasers on silicon using transfer printing of epitaxial layers," Nat. Photonics **6**, 610–614 (2012).

35. A. Leverrier, "Composable security proof for continuous-variable quantum key distribution with coherent states," Phys. Rev. Lett. **114**, 070501 (2015).

36. I. Derkach and A. Hajomer, "Data summary for "Chip-based 16 GBaud continuous-variable quantum key distribution"," Zenodo, (2026), https://zenodo.org/records/19698433.